ACS Catalysis

Article

Metal Organic Framework Derived Synthesis of Cobalt Indium Catalysts for the Hydrogenation of CO2 to methanol

Alexey Pustovarenko, Alla Dikhtiarenko, Anastasiya Bavykina, Lieven E. Gevers, Adrian Ramirez, Artem Russkikh, Selvedin Telalovic, Antonio Aguilar, Jean Louis Hazemann, Samy Ould-Chikh, and Jorge Gascon

ACS Catal., **Just Accepted Manuscript** • DOI: 10.1021/acscatal.0c00449 • Publication Date (Web): 03 Apr 2020

Metal Organic Framework Derived Synthesis of Cobalt Indium Catalysts for the Hydrogenation of CO_2 to methanol

Alexey Pustovarenko,[†] Alla Dikhtiarenko,[†] Anastasiya Bavykina,[†] Lieven Gevers,[†] Adrian Ramírez,[†] Artem Russkikh,[†] Selvedin Telalovic,[†] Antonio Aguilar,[§] Jean-Louis Hazemann,[§] Samy Oud-Chikh[†] and Jorge Gascon[†,]*

[†] King Abdullah University of Science and Technology, KAUST Catalysis Center (KCC), Advanced Catalytic Materials, Thuwal 23955, Saudi Arabia

[§] Néel, UPR2940 CNRS, University of Grenoble Alpes, F-38000 Grenoble, France

KEYWORDS: metal-organic framework derived route, direct CO_2 hydrogenation, methanol synthesis, indium oxide, cobalt oxide.

ABSTRACT

Methanol synthesis by means of direct CO_2 hydrogenation has the potential to contribute to climate change mitigation by turning the most important greenhouse gas into a commodity. However, for this process to become industrially relevant, catalytic systems with improved activity, selectivity and stability are required. Here we explore the potential of metal-organic frameworks (MOF) as precursors for synthesis of Co_3O_4-supported In_2O_3 oxide composites for the direct CO_2 hydrogenation to methanol. Stepwise pyrolytic-oxidative decomposition of indium-impregnated ZIF-67(Co) MOF affords the formation of a nanostructured In_2O_3@Co_3O_4 reticulated shell composite material able to reach a maximum methanol production rate of 0.65 $g_{MeOH}\cdot g_{cat}^{-1}\cdot h^{-1}$ with selectivity as high as 87% over 100 h on stream. Textural characteristics of the sacrificial ZIF-67(Co) matrix and In-loading were found to be important variables for optimizing the catalyst performance such as induction time, methanol productivity and selectivity. The structural investigation on the catalytic system reveals that the catalyst undergoes reorganization under reaction conditions, transforming from a Co_3O_4 with amorphous In_2O_3 shell into $Co_3InC_{0.75}$ covered by a layer consisting of a mixture of amorphous CoO_x and In_2O_3 oxides. Structural reorganization is responsible for the observed induction period, while the amorphous mixed cobalt indium oxide shell is responsible for the high methanol yield and selectivity. Additionally, these results demonstrate the tunable performance of MOF-derived In_2O_3@Co_3O_4 catalyst as a function of the reaction conditions which allows to establish a reasonable trade-off between high methanol yield and selectivity in a wide temperature and pressure window.

1. Introduction

Anthropogenic CO_2 emissions increase year by year, with very serious consequences for our climate. In order to solve these environmental and energy issues, intensive research is being carried out into technologies that may eventually turn our economy into a low-carbon one.[1] In this scenario of a circular carbon economy, carbon dioxide is viewed as an alternative resource that can be recycled to produce valuable chemicals and fuels,[2-4] turning, in such a way, waste to wealth. Among the potential products derived from CO_2, methanol has attracted particular attention due to its relevance not only as an alternative fuel [5-6] but also as a convenient chemical feedstock.[7-11]

Indeed, methanol synthesis through direct hydrogenation of CO_2, using pure H_2 and CO_2 as starting materials, is considered to be a very promising strategy to utilize CO_2 when green hydrogen (produced *via* electrolysis using renewable energy) is available.[2,11-13] At the current stage, the Cu-ZnO-Al_2O_3 catalyst commercially used in the production of methanol from synthesis gas ($CO/CO_2/H_2$) is the benchmark.[14-15] In direct CO_2 hydrogenation, this catalyst is able to drive, to some extent, the production of methanol, however exhibiting low selectivity and fast deactivation caused by competitive reverse water gas shift reaction (RWGS).[15-17] To address these selectivity and stability issues, a number of multi-metallic composite systems have been proposed, *i.e.* CuO/ZrO_2, $CuO/ZnO/ZrO_2$, $CuO/ZnO/Ga_2O_3$, $Cu/ZnO/ZrO_2/Al_2O_3/SiO_2$,[18-21] and their doped variations (*i.e.*, by Ag, Au, Pt, Pd, Rh promotors).[22-27] These mix-component systems are able to convert CO_2 to methanol with high selectivities at low conversions per pass, such as in case of Cu@ZnO core-shell (S_{MeOH} ~ 100 %, X_{CO2} conversion of 2.3 %)[21] or Au-doped ZnO-ZrO_2 (S_{MeOH} ~ 100%, X_{CO2} ~ 1.5 %).[27] Contrariwise, when higher CO_2 conversions are targeted, low methanol selectivities are usually achieved. This is the case, for instance, for Cu-K/Al_2O_3 (S_{MeOH} = 2 % at X = 29)[28] and for Cu/Zn/Al/Y (S_{MeOH} = 52 % at X = 27).[29]

Among recent studies on simpler metal oxide systems featuring higher stability, density functional theory (DFT) calculations predict that methanol synthesis *via* CO_2 hydrogenation is favored over In_2O_3 surfaces.[30] The proposed catalytic mechanism involves cyclic generation of oxygen vacancies on In_2O_3 by H_2 and their replenishment *via* CO_2 activation. Later, Sun *et. al.*[31] experimentally proved the superior activity of In_2O_3 for CO_2 hydrogenation to methanol. When In_2O_3 supported is supported on ZrO_2, further improvements in catalytic performance have been reported: at low conversion levels, almost 100% selectivity to methanol with space time yield (STY) of 0.32 $g_{MeOH}{\cdot}g_{cat}^{-1}{\cdot}h^{-1}$ and stable performance over 1000 h on stream can be achieved.[32] In light of recent advances made in In-based bimetallic formulations[33] with improved catalytic merits and inspired by the drastic importance of carrier supports in such catalytic systems, Bavykina *et. al.*[34] prepared a pre-catalyst consisting in In_2O_3 supported on Co_3O_4 by means of reverse co-precipitation. The resulting In@Co system catalyzes methanol formation *via* CO_2 hydrogenation with selectivities above 80% and productivity of 0.86 $g_{MeOH}{\cdot}g_{cat}^{-1}{\cdot}h^{-1}$, at conversion levels close to thermodynamic equilibrium.

It is well known that, in heterogeneous catalysis, the preparation method significantly affects catalytic performance.[25] Over the last decade, particular interest has been paid to Metal-Organic Framework (MOF)-supported and MOF mediated synthetic approaches to prepare highly effective catalysts for a variety of catalytic transformations.[35-37] Being microporous crystalline materials with a tailored arrangement of metal-centers and bridging linkers,[38] MOFs dispose a system of pores that can be loaded with active components offering an optimal distribution of active sites. For instance, an encapsulation of Cu and/or ZnO nanoparticles within UiO-66(Zr) [39,40] resulted in highly active catalyst showing an 8-fold enhanced yield and 100% selectivity towards methanol (albeit at very low conversions, where the effect of RWGS is minimized) when compared to the

benchmark Cu/ZnO/Al_2O_3. Besides the promising perspectives of MOF-supported catalysts, recent investigations reveal the advantages in preparation of highly efficient heterogeneous catalytic materials from metal-organic framework supports/precursors by means of thermal decomposition.[37,41-42] MOF-derived nanocomposite materials, *i.e.* MOF-derived carbons and oxides, feature a range of advantages, such as high specific area, porosity and excellent distribution of the active component within the host matrix, compared to similar materials prepared by co-precipitation or impregnation methods.[37,42]

In light of these results, here we explore the MOF mediated route for the preparation of a highly efficient Co_3O_4-supported In_2O_3 catalyst in line with our previous findings on this inorganic system.[34] The impregnation of ZIF-67(Co) with indium, followed by thermal decomposition, results in the formation of In@Co oxide composite materials with enhanced catalytic behavior in CO_2 hydrogenation to methanol, revealing higher methanol yields, selectivities and significantly shortened induction times (10 h *vs*. 30 h observed for In@Co prepared by co-precipitation).[34] The influence of the crystal size of the parent ZIF-67(Co) and the amount of loaded indium on the catalytic performance has been thoroughly studied. Moreover, the importance of two-step thermal treatment (pyrolysis followed by calcination) for In-impregnated ZIF-67(Co) material in order to obtain highly performing catalysts is also discussed in detail.

2. Experimental section

2.1. Materials

All chemicals were purchased from Sigma-Aldrich and used as received. Commercial Cu-ZnO-Al_2O_3 methanol synthesis catalyst was obtained from Alfa Aesar™ (composition: 60-68% CuO, 22-26% ZnO, 8-12% Al_2O_3, 1-3% MgO).

2.2. Synthetic procedures

Synthesis of 300 nm ZIF-67(Co). The synthesis of ZIF-67(Co) with a crystallite size around 300 nm was performed in accordance to the previously reported method.[43-44] Following the typical synthetic protocol, 2.933 g (10 mmol) of $Co(NO_3)_2{\cdot}6H_2O$ and 6.489 g (79 mmol) of 2-methylimidazole (MeIm) were separately dissolved in 200 mL of methanol. The MeIm-containing clear solution was rapidly poured into the pink solution of the cobalt salt. The mixture was stirred for 12 min and then kept standing for 24 h to allow precipitation to take place. The bright purple product was collected by centrifugation, washed several times with methanol, and dried at 423 K for 10 h under vacuum.

Synthesis of 22 nm ZIF-67(Co). ZIF-67(Co) with a crystallite size around 22 nm was obtained through modulated synthesis with triethylamine (TEA). In typical procedure, 0.582 g (2 mmol) of $Co(NO_3)_2{\cdot}6H_2O$ and 4.866 g (60 mmol) of 2-methylimidazole (MeIm) were dissolved in 400 mL methanol. Afterwards, 5 mL of triethylamine was added to the vigorously stirred mixture and stirring continued for 15 min. When precipitation started, the mixture was kept steady for 24 h. The product was collected by centrifugation, washed several times with methanol, and dried at 423 K for 10 h under vacuum.

Synthesis of MOF-derived In@Co catalysts by incipient wetness impregnation method. The catalysts were prepared by incipient wetness impregnation (IWI) in the following manner: 1 g of activated ZIF-67(Co) was impregnated with 3 mL of aqueous indium nitrate solution of different indium concentrations as stated in Table S1 and then dried under vacuum at 100 °C overnight. For thermal treatment, an In-impregnated ZIF-67(Co) precursor sample was transferred into a quartz reactor (L = 1 m and ID = 5 cm), vertically inserted into tubular oven equipped with temperature (Nabertherm) and mass-flow controllers (Bronkhorst® High-Tech), and followed by two thermal

treatment steps in sequential order: first, pyrolysis at 600 °C (1 °C·min^{-1}, 4 h) in nitrogen flow (25 mL·min^{-1}), then calcination at 400 °C (1 °C·min^{-1}, 2 h) in air flow (25 mL·min^{-1}). The obtained In@Co samples are denoted as ***a***In:***b***Co(***x***) where ***x*** is the crystal size of the ZIF-67(Co) precursor, ***a*** and ***b*** indicate the desired In:Co molar ratio.

2.3. Characterization methods

Powder X-ray diffraction (PXRD) patterns were acquired on a Bruker D8 Advance operated at 30 kV and 30 mA using monochromatic Cu-Kα (λ = 1.5418 Å) radiation, a scan speed of 15 s per step and a step size of 0.05° on 10 – 80° 2θ range. For phase analysis of reacted catalysts, the X-ray diffraction data were measured under inert atmosphere using an airtight sample holder which was loaded in a glove box under Ar atmosphere. The crystalline phase was identified with the help of the PDF-4+ (2019) crystal database. The profile matching of all PXRDs with expected crystalline phases was confirmed by Pawley fitting [45] and quantitative estimation of the phases was obtained by Rietveld refinement using TOPAS V5 (academic version) software.[46] The results of refinements are provided in Fig. S28.

Nitrogen adsorption experiments were carried out at 77 K using a Micromeritics ASAP 2040 instrument. Before the measurements, the ZIF-67(Co) samples were degassed at 150 °C for 10 hours and the calcined products were degassed at 100 °C for 10 hours.

Thermogravimetric data (TG) were collected in nitrogen and air atmospheres using a Mettler Toledo thermal analyzer at a heating rate of 5 °C·min^{-1} in the 25 – 950 °C temperature range and at a dynamic gas flow rate of 20 mL·min^{-1}.

Scanning electron microscopy (SEM) imaging was performed with secondary electrons on a FEI TENEO VS microscope using 5 kV acceleration voltage and 5 mm working distance. The crystal

size distribution for each sample was obtained analyzing several images recorded at different magnifications using ImageJ software.[47]

The annular Dark-Field scanning transmission electron microscopy (ADF-STEM) in conjunction with Electron Energy Loss Spectroscopy (EELS) study was carried out with a Cs-Probe Corrected Titan microscope (Thermo-Fisher Scientific) which was also equipped with a GIF Quantum of model 966 from Gatan Inc. (Pleasanton, CA). STEM-EELS analysis was performed by operating the microscope at the accelerating voltage of 300 kV, using a convergence angle α of 17 mrad and a collection angle β of 38 mrad. Spectrum-imaging dataset includes the simultaneous acquisition of zero-loss and core-loss spectra (DualEELS) using a dispersion of 0.5 eV/channel and were recorded using a beam current of 0.2 nA and a dwell time of 20 ms/pixel. The Co $L_{2,3}$-edge, In $M_{4,5}$-edge, and O K-edge were selected to build the chemical maps. Carbon K-edge was acquired by continuously scanning a $Co_3InC_{0.75}$ nanoparticle while simultaneously acquiring 10 Dual-EELS spectra (frame time = 10 s) using a dispersion of 0.1 eV/channel. The energy scale of all high loss EELS spectra was referenced to the zero-loss peak. Carbon K-edge spectra were normalized using ATHENA software.[48] Typically, the specimens were prepared by dispersing the catalyst in methanol under ultrasound irradiation during 30 min and placing several drops of the resulting dispersion on the copper grids having a carbon layer. For the particular study of carbon K-edge, a nickel grid with a lacey-carbon layer was used to record EELS spectra without the interference of the supporting carbon. The QSTEM software[49] was used to simulate high-resolution lattice images of the $Co_3InC_{0.75}$ nanoparticle along the <101> zone axis using a slab thickness of 4.8 nm. For the microscope parameters, we used an accelerating voltage of 300 kV, a spherical aberration coefficient (C_s) of 1.0 mm, a defocus (df) of -1.7 nm, a chromatic aberration coefficient (C_c) of 1 mm, an energy spread (dE) of 1.0 eV, a convergence angle α = 17 mrad, and

a detector collection angle of [63, 200] mrad. *Ab-initio* simulations of the carbon K-edge were performed using the FDMNES package. The FDMNES code features mono-electronic calculations, which are carried out in real space with Hedin-Lundqvist exchange-correlation potential and using clusters built around each non-equivalent absorbing atom.[50-51] The finite-difference method (FDM) implemented in the FDMNES code was used since the latter is a full potential method that introduces no approximation on the shape of the potential. To take into account the core-hole lifetime and other multielectronic phenomena occurring in the absorption process, a convolution procedure was applied to the calculated spectra. At the Fermi level, the Lorentzian (FWHM) width was set to 0.16 eV. The instrumental energy resolution was taken into account by further convoluting the calculated spectra with a Gaussian broadening of 1.5 eV width.

The XAS experiments were performed at CRG-FAME beamline (BM30B) at the European Synchrotron Radiation Facility (ESRF). The ring is operated at 6 GeV with a nominal current of 200 mA in 7/8+1 mode. The beamline is equipped with a liquid-nitrogen-cooled doubled crystal Si(220) monochromator surrounded by two Rh-coated mirrors for harmonic rejection. The beam size on the sample is 240×110 μm (H×V, FWHM). Cobalt K-edge spectra were collected in fluorescence mode using a CANBERRA 30-elements Ge solid state detector. Indium K-edge spectra were collected in transmission mode using silicon diodes to measure the incident and transmitted beam intensities. The monochromator was energy calibrated measuring the cobalt and indium K absorption edges using a metallic cobalt and indium foil respectively. First maximum of the 1st derivative of the absorption cobalt K-edge was set at 7709 eV and 27940 eV for indium K-edge. The data acquisitions of reacted catalysts were performed *ex-situ* either in fluorescence or transmission mode with the samples retrieved inside a glove box and loaded into a XAS cell dedicated for air-sensitive compounds. Non-air sensitive fresh catalyst and reference compounds

were handled outside of glove box and measured in fluorescence mode using conventional sample holder. All samples were diluted with boron nitride and pressed into pellets to optimize the effective XAFS edge-step. On average four scans were acquired for each sample to improve the signal to noise level of the data. All XAS data were analyzed using the HORAE package, a graphical interface to the AUTOBK and IFEFFIT code.[48] The EXAFS spectra were obtained after performing standard procedures for pre-edge subtraction, normalization, polynomial removal, and wavevector conversion. The amplitude factors (S_0^2) were fitted to the EXAFS spectra recorded for a Co metallic foil and an In_2O_3 powder (Table S3 and Figure S18). S_0^2 were determined to be 0.73 ± 0.04 and 0.99 ± 0.03 for Co and In, respectively.

CHN elemental analyses on selected samples were performed using a Thermo Flash 2000 Organic Elemental Analyzer with the detection limits of 0.2 % (w/w) for carbon, 0.1% for nitrogen and 0.08% for hydrogen. For the analysis of the used catalysts, the corresponding samples were transferred unopened from the reactor to the glovebox and were kept under Ar atmosphere. To avoid undesired reaction of the used catalysts with air, all samples were sealed in tin sample crucibles in a glove box under Ar atmosphere. For each sample three individual measurements were performed and the mean was calculated as a final result.

X-ray fluorescence measurements (XRF) were performed on a HORIBA XGT-700 XRF analyzer. For every measurement, three different spots were analyzed for each sample with a total acquisition time of 1500 s per sample.

2.4. Catalytic testing in CO_2 hydrogenation to methanol

Catalytic tests were performed using a parallel reactor system Flowrence® from Avantium consisting of 16 tubular fix-bed reactors installed in a furnace and operated at one mixed feed gas flow which is distributed over 16 channels with a relative standard deviation of 2%. 50 mg of the

catalyst with particle fraction between 150 μm and 250 μm was loaded onto the stainless-steel tube reactor (30 cm long with 2 mm of internal diameter) preliminary filled with 9.5 cm bed of coarse SiC (particle grit 40, 300 μL) in order to ensure the isothermal zone for the catalytic bed. Before the catalytic test, the catalysts were pretreated in-situ under N_2 at 300 °C for 1 hour. Then, the reactors were pressurized with a mixed feed containing 20 vol.% of CO_2 and 80 vol.% of H_2 to 50 bar using a membrane-based pressure controller. In addition, 0.5 mL/min of He was mixed with the feed and used as internal standard. The products were analyzed with an Agilent 7890B chromatograph equipped with two loops, where one was connected to the Column 5 HaysepQ6 Ft G3591-80013 and TCD and the second Gaspro 30M, 0.32 mm OD column followed by FID.

Conversion (X, %), space time yield (STY, $g_i \cdot g_{cat}^{-1} \cdot h^{-1}$), and selectivity ($S$, %) are defined as follows:

$$X_{CO_2} = \left(1 - \frac{C_{He,blk} \cdot C_{CO_2,R}}{C_{He,R} \cdot C_{CO_2,blk}}\right) \cdot 100$$

$$S_i = \frac{\left(\frac{C_{i,R}}{C_{He,R}}\right)}{\left(\frac{C_{CO_2,blk}}{C_{He,blk}} - \frac{C_{CO_2,R}}{C_{He,R}}\right)} \cdot 100$$

$$STY_i = \frac{\frac{X_{CO_2}}{100} \cdot \frac{S_i}{100} \cdot M_i \cdot GHSV}{22.4}$$

where $C_{He,blk}$, $C_{He,R}$, $C_{CO2,blk}$, $C_{CO2,R}$ are the concentrations determined by GC analysis of He in the blank, He in the reactor effluent, CO_2 in the blank, and CO_2 in the reactor effluent, respectively,

$C_{i,R}$ is the concentration of the product determined by GC, M_i is the molecular weight of product *i* and GHSV is CO_2 gas hourly space velocity in $L \cdot g_{cat}^{-1} \cdot h^{-1}$.

Carbon balance in all experiments accounted for more than 97.8% of the total carbon input whereas a small amount of carbon trapped in form of mixed metal carbide was comparatively modest. Reproducibility of the catalytic experiment was carried out for representative sample and was found to be deviating within 1.7% relative experimental error.

3. Results and Discussion

In our study we explored ZIF-67(Co) framework as a precursor material for the preparation of indium loaded MOF-derived cobalt oxide supported catalysts (In@Co). ZIF-67(Co) is a zeolitic imidazolate framework formed by cobalt and 2-methylimidazole (MeIm) featuring a porous architecture with sodalite (sod) topology (Fig. 1A-B), and has been chosen as a sacrificial material due to its high cobalt content (26 wt.% Co). We synthesized two types of ZIF-67(Co) samples with different crystal sizes in order to evaluate the effect they may induce on the performance of the derived In@Co catalysts. Thus, applying a modulated synthesis protocol, ZIF-67(Co) with average crystal sizes of 20 nm and 300 nm were obtained. These samples are referred as ZIF-67(Co)-20 and ZIF-67(Co)-300, respectively. As it can be observed from Figures 1D-E (insets) and S1, both samples possess narrow size distribution profiles. To confirm matching of ZIF-67(Co)-20 and -300 with the ZIF-67 structure, powder X-ray diffraction analyses have been performed and compared in Figure 1C. Both materials reveal the typical reflections attributed to the cubic ZIF-67 structure.[52-53] However, the notable broadening of the peaks in case of ZIF-67(Co)-20 indicates that the sample has a smaller crystal size compared to the ZIF-67(Co)-300.

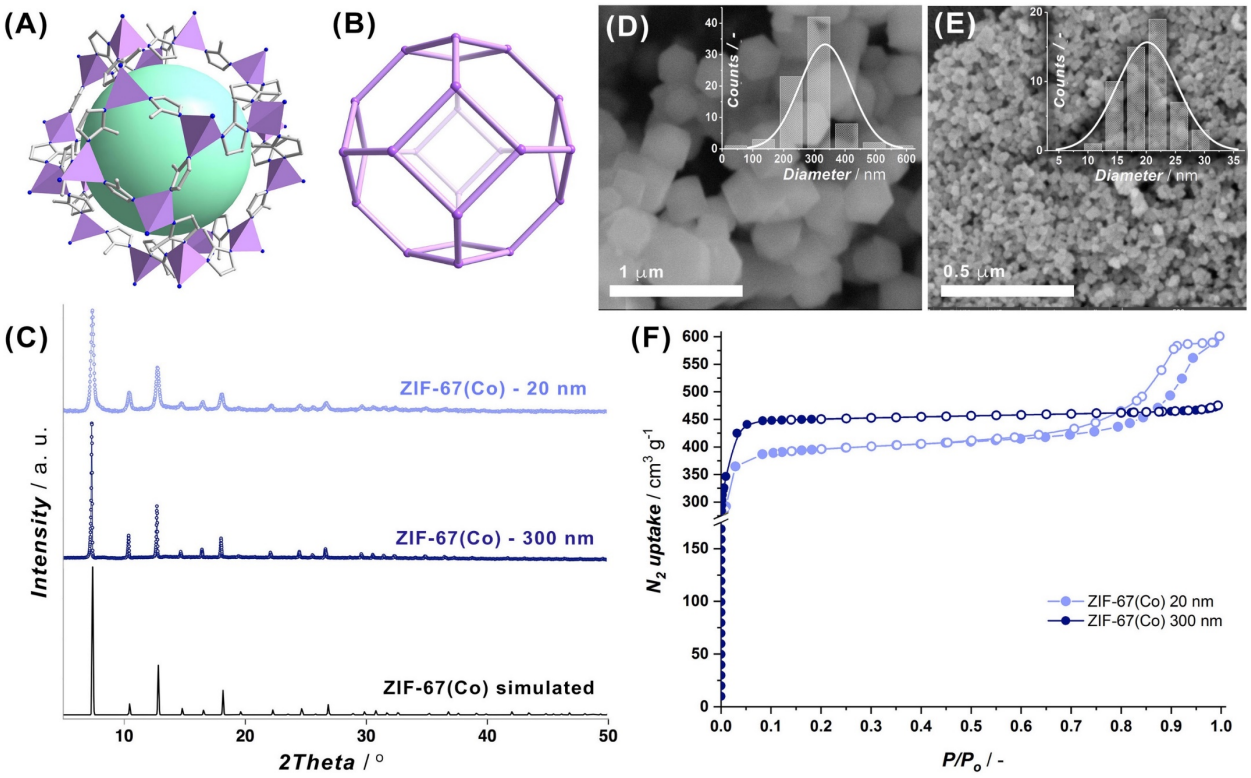

Figure 1 (*double column*). (A) Cage structure of ZIF-67(Co) and (B) its topological view reveling sod fragment. (C) Powder X-ray diffraction patterns compared to theoretically expected ZIF-67(Co) (cubic I-43m);[53] (D-E) SEM micrographs along with size distribution histograms (insets) and (F) N_2 adsorption isotherms acquired at 77 K for ZIF-67(Co) precursor samples of 300 ± 85nm (blue symbols) and 20 ± 5 nm (violet symbols) crystal sizes, respectively. On the isotherm graph the filled markers correspond to the adsorption curve and the hollow ones to desorption branch.

In order to evaluate the textural properties of the ZIF-67(Co)-20 and -300 materials with different crystal sizes, nitrogen adsorption experiments have been carried out. Figure 1F shows corresponding nitrogen sorption isotherms for both 20 nm and 300 nm ZIF-67(Co) precursors. The BET analyses reveal very close microporous surface areas of 1579 and 1566 $m^2 \cdot g^{-1}$ for ZIF-67(Co)-300 and -20, respectively (Table S2). Notably, the N_2 adsorption isotherm for ZIF-67(Co)-300

exhibits a typical type I shape, corroborating the fully microporous nature of the material, whereas ZIF-67(Co)-20 features IV-type with a hysteresis loop at high relative pressures, most likely derived from interparticle condensation of N_2.[54-55]

Considering that in our study the catalysts are prepared by thermal decomposition of ZIF-67(Co), thermogravimetric analysis is a necessary tool to determine optimal conditions for the treatment. ZIF-67(Co) decomposes in nitrogen atmosphere at temperatures above 550 °C (Fig. S2) yielding Co nanoparticles of ~ 4.7 nm size highly dispersed within a carbon matrix, which mainly consists of graphite nanotubes (Fig. S3). The PXRD data for the Co@C material derived from pristine ZIF-67(Co) show (Fig. S4) broad peaks originated from graphite (*hcp* C allotrope) and metallic Co (*fcc* form, α-Co allotrope) phases. Notably, the pyrolysis of ZIF-67(Co) at 600 °C results in the formation of α-Co phase,[56] allotrope which is expected to be thermodynamically favored at temperatures above 417 °C and exists as a metastable phase at room temperature.[56] In contrast, the decomposition of ZIF-67(Co) in air flow proceeds in two steps (Fig. S2): *i*) oxidative destruction of the framework with a weight loss of *ca*. 63 wt.% yielding Co_3O_4 as main decomposition product at 400 °C; and *ii*) transformation of Co_3O_4 to CoO [57] occurring at 900 °C with additional 2.7 wt.% mass loss. In a similar way, Co@C decomposes during the calcination step (Fig. S5), losing 43 wt.% due to carbon oxidation resulting in Co_3O_4 at 400 °C. The product obtained by two-step decomposition comprises uniform nanoparticles of 5.8 nm average size (Fig. S6) with the spinel Co_3O_4 structure (Fig. S7).

Typically, we prepared In@Co catalysts in three steps: *i*) incipient wetness impregnation of ZIF-67(Co) with an aqueous $In(NO_3)_3$ solution; *ii*) pyrolysis of In@ZIF-67(Co) at 600 °C in nitrogen; *iii*) calcination of the obtained product at 400 °C in flow of synthetic air. Upon IWI step, ZIF-67(Co) crystals undergo agglomeration with visible sealing at the edges of the particles (Fig. S8).

Thereafter, during the pyrolysis step, In@ZIF-67(Co) transforms into mixture of freestanding spherical particles of about 12 nm size, which tend to sinter under the electron beam, and agglomerations of smaller ones with a mean size of about 10 nm (Fig. S9). Qualitative analysis performed on the XRD pattern indicates a mixture of nanosized α-Co and mixed-metal carbide, $Co_3InC_{0.75}$ phases, where the carbide phase is dominant (Fig. S10). This observation supports the effectiveness of IWI method and suggests high dispersion of the loaded In component. At the last step of catalyst preparation, the pyrolyzed product has been calcined in a stream of air at the temperature suitable for conversion to oxide form (*i.e*. 400 °C).

The resulting catalyst, having an In:Co molar ratio of 3:8 and referred to as **3**In@**8**Co(300), consists of 5-10 nm sized oxide nanoparticles (Fig. S11) developing a considerable high surface area of 107 $m^2 \cdot g^{-1}$. Notably, the XRD pattern reveals broad diffraction lines attributed only to the Co_3O_4 phase. This is also in accordance with the EXAFS spectroscopy applied at Co K-edge, which reveals the characteristic fingerprint of the Co_3O_4 crystal structure and is further supported by subsequent fitting of the EXAFS data (details in supplementary information, Table S3, Figs. 18A-B). An interesting observation is the absence of any In-derived compounds in the PXRD pattern, although the sample was calcined at 400 °C (Fig. S12). The state of indium in the **3**In@**8**Co(300) pre-catalyst was thus refined by EXAFS spectroscopy applied at the indium K-edge. The spectrum of **3**In@**8**Co(300) pre-catalyst is shown on Figs. 2(A)-(B) together with the spectrum of a crystalline In_2O_3.

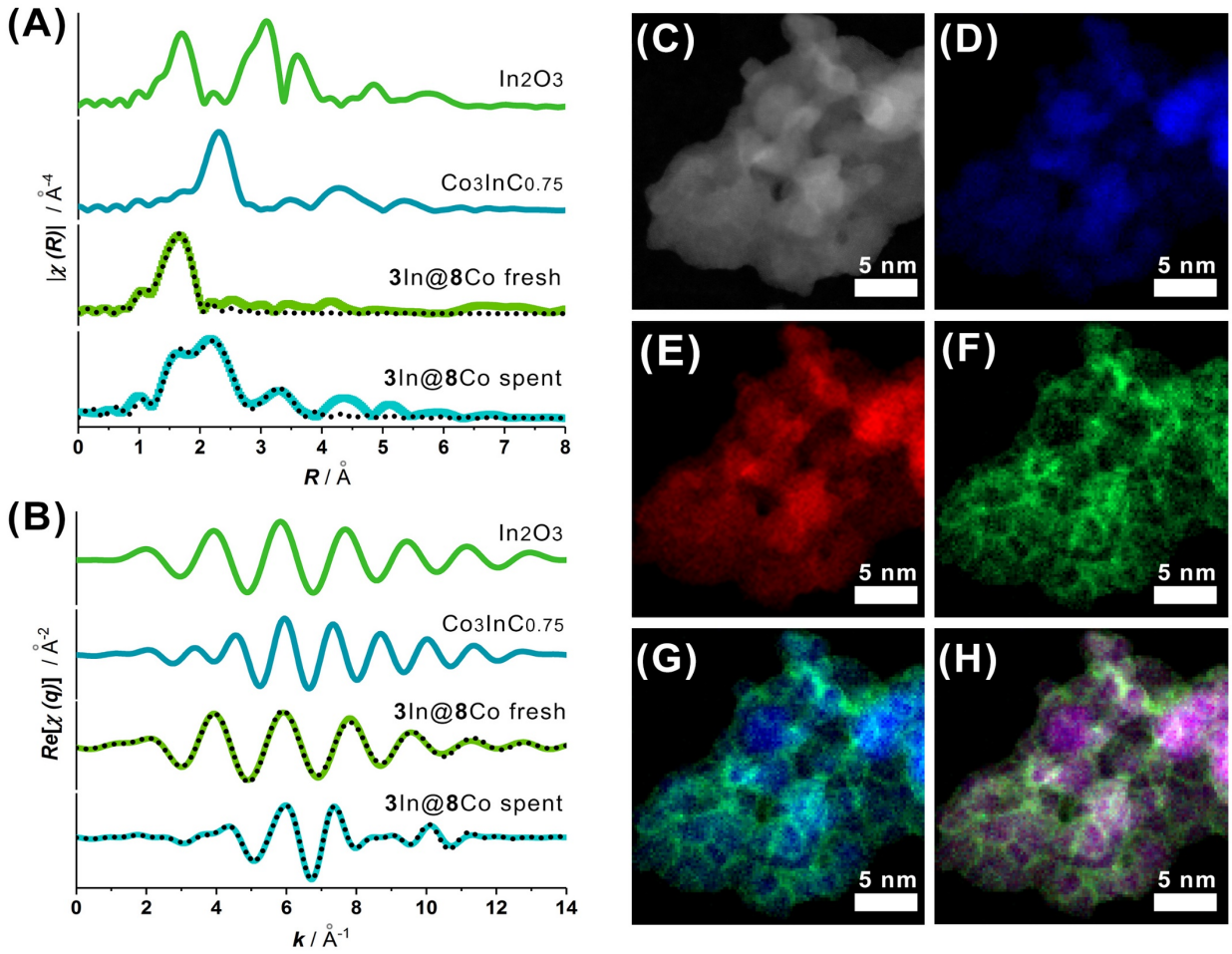

Figure 2 (*double column*). (A) Magnitude of the Fourier transform for the EXAFS $k^3 \cdot \chi(k)$ functions acquired at In K-edge for In_2O_3, $Co_3InC_{0.75}$, **3**In@**8**Co(300) catalyst before and after CO_2 hydrogenation reaction and, (B) their related back Fourier transforms (real part) applied within their respective R-range for EXAFS fitting. Solid line represents experimental data whereas dotted line corresponds to fit results conducted with [1.1–2.5] Å and [1.2–3.6] Å R-range together with a [2.9–12.8] $Å^{-1}$ and [3.8–10.4] $Å^{-1}$ k-range, respectively for **3**In@**8**Co(300) catalyst before and after reaction. (C) ADF-STEM image and elemental mappings for **3**In@**8**Co(300): (D) Co, (E) O, (F) In maps and superimposed (G) Co/In maps and (H) Co/In/O maps.

Qualitative assessment of the FT-EXAFS spectra for the In_2O_3 reference (without phase correction), indicate a main peak at 1.7 Å attributed to In-O scattering and several peaks between 2.5 and 4.3 Å assigned mainly to In-In path with some minor contributions from In-O scattering and some multiple scattering processes.[58] In contrast, the FT-EXAFS of the **3**In@**8**Co(300) pre-catalyst show only one prominent peak centered around 1.6 Å which is similar to the low-R peak of the In_2O_3 FT-EXAFS spectrum. The lack of contribution from more distant coordination shells (*e.g*. In-In scattering path, Table S3) is associated with deficiency of the long-range order and proves the amorphous nature of the indium component in the **3**In@**8**Co(300) pre-catalyst. Quantitative EXAFS fitting of the first shell with a single In-O scattering path provides a coordination number of 6.3 ± 0.7 at a bonding distance of 2.14 ± 0.01Å, consistent with an octahedral coordination (Table S3). The distribution of the indium oxide within the sample is further highlighted by ADF-STEM imaging and EELS elemental mapping (Figs. 2(C)-(H): the amorphous indium oxide covers homogeneously the 5 nm Co_3O_4 nanoparticles as a thin layer.

The catalytic performance of ZIF-67(Co)-derived indium containing catalysts in CO_2 hydrogenation has been evaluated at 300 °C and 50 bar with a constant 20%CO_2/80%H_2 feed flow. The kinetic profile of the reaction on **3**In@**8**Co(300) catalyst (Fig. 3A) shows an induction period of 20 h until it reaches 0.4 $g_{MeOH}{\cdot}g_{cat}^{-1}{\cdot}h^{-1}$ methanol productivity. As the reaction proceeds, the methanol selectivity stabilizes at 63% with CO and CH_4 by-product selectivities of 27% and 9%, respectively (Fig. 3B, Fig. S29). Overall, the CO_2 conversion is stable over 100 h on steady state performance, yielding an STY of 0.5 $g_{MeOH}{\cdot}g_{cat}^{-1}{\cdot}h^{-1}$ for methanol.

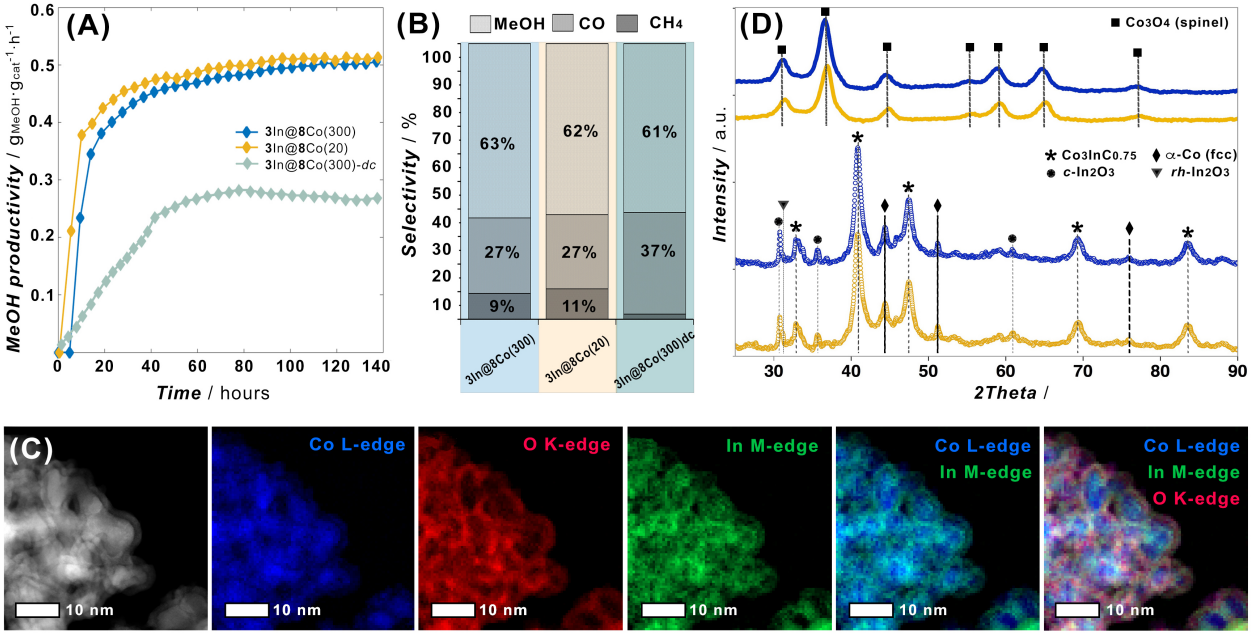

Figure 3. (*double column*). (A) Kinetic profile of evolution MeOH space time yield with time and (B) MeOH, CO and CH_4 selectivities at time-on-stream (*TOS*) of 100 h over **3**In@**8**Co(300) (orange line), **3**In@**8**Co(20) (navy line) and **3**In@**8**Co(300)-*dc* (turquoise line) catalysts at X_{CO2} of 18%, 19% and 13%, respectively. (B) MeOH, CO and CH_4 selectivities on stable plateau of the kinetic profile (100 h) on studied catalysts. Reaction conditions: 80%H_2-20%CO_2 feed; T = 300 °C, P = 50 bar, m_{cat} = 50 mg, GHSV = 15600 h^{-1}. (C) ADF-STEM imaging and elemental mapping for **3**In@**8**Co(300) after the reaction: (from left to right) ADF-STEM image, Co, O, In maps and superimposed Co/In maps and Co/In/O maps. (D) XRD patterns for fresh (top) and spent (bottom) **3**In@**8**Co(300) (orange) and **3**In@**8**Co(20) (navy) catalysts compared to identified phases: Co_3O_4 (■), $Co_3InC_{0.75}$ (*), α-Co (*fcc*,◆), *c*-In_2O_3 (cubic,●) and *rh*-In_2O_3 (rhombohedral,▼).

As previously reported by our group [34] and characterized below (vide infra), the induction period is associated with the formation of the active phase by a solid reaction between the indium oxide layer with its supporting cobaltite phase. Having a higher external surface area in the starting

sacrificial ZIF-67(Co) is expected to enhance the contact between indium and cobalt oxides and to increase substantially the formation rate of the active phase. To this end, another ZIF-67(Co) support with smaller crystal size - ZIF-67(Co)-20nm – was used to improve the dispersion of the In-component. The impregnation at the same In:Co molar ratio (3:8) followed by a two steps thermal decomposition resulted in a material possessing 119 $m^2 \cdot g^{-1}$ of total surface area, **3**In@**8**Co(20) (Table S4). The kinetic profile of reaction expressed in STY_{MeOH} on **3**In@**8**Co(20) catalyst is shown on Figure 3A and compared to **3**In@**8**Co(300) behavior at the same reaction conditions. As anticipated, **3**In@**8**Co(20) catalyst obtained from MOF with smaller particle size shows considerably reduced induction period of 10 h versus 19 h (STY_{MeOH} of 0.38 $g_{MeOH} \cdot g_{cat}^{-1} \cdot h^{-1}$) observed in case of **3**In@**8**Co(300). However, both catalysts demonstrate similar selectivities towards MeOH (~63%) and by-products (CO, ~27% and CH_4, ~9-11%) reaching stable STY values of 0.52 $g_{MeOH} \cdot g_{cat}^{-1} \cdot h^{-1}$ for methanol production.

To gain some insights on the structural composition of **3**In@**8**Co after the catalytic run, PXRD analyses were performed for reacted catalysts which were expressly protected under inert atmosphere in order to exclude any possible phase transformation caused by exposure to air. Comparison of the diffraction patterns for fresh and spent catalysts along with the *d*-spacing positions for identified crystalline phases is shown in Figure 3D. Evidently, both catalysts undergo a phase transformation – from crystalline spinel with amorphous In_2O_3 to a complex mixture consisting of mixed-metal carbide $Co_3InC_{0.75}$, α-Co (*fcc* form), cubic allotrope of In_2O_3 (*c*-In_2O_3), traces of rhombohedral In_2O_3 phase (*rh*-In_2O_3) and both CoO polymorphs (Fig. S13). Besides the evidences gained from PXRD, these structural transformations were confirmed by In and Co K-edge EXAFS analyses performed *ex-situ* for the catalyst before and after catalytic process (Figs. 2(A)-(B), S17(A)-(B), Table S3). Interestingly, the hexagonally packed *rh*-In_2O_3 is a metastable

polymorphic form of indium oxide which irreversibly transforms, under elevated temperatures and pressures of 0.1 MPa-3GPa, to the more stable cubic form.[59-60] Additionally, it is known that in strongly reductive atmospheres, such as CO and H_2, the allotrope transformation proceeds following the same pathway - *rh*-In_2O_3 → *c*-In_2O_3 meanwhile the reverse transformation happens only at high energy input.[61] Extrapolating the observation, one of the processes occurred during the catalytic run is recrystallization of amorphous In_2O_3: firstly, to *rh*-In_2O_3 and then to more stable *c*-In_2O_3. However, a minor part of *rh*-In_2O_3 is still present after catalysis. Simultaneously with the formation of crystalline In_2O_3, the Co_3O_4 phase undergoes reductive transformation following the sequence Co_3O_4 → CoO → Co which results in nanoparticles of α-Co (*fcc*) polymorph and traces of CoO (*hcp*/*fcc*) phases (Fig. 3D, Fig. S13B). Finally, the third and more peculiar component found to be formed is a mixed metal carbide, $Co_3InC_{0.75}$ (Fig. 3D). Since the reductive atmosphere of reaction should drive the transformation of oxides to their corresponding metallic phases, the occurrence of this carbide is attributed to the reductive transformation under carbon-rich atmospheres better described as carburization process.

Imaging operated by ADF-STEM microscopy and performed on the **3**In@**8**Co(300) material after the catalytic run shows also that the catalyst undergoes textural changes along with phase reorganization. The vast majority of the sample is a composite formed from aggregated nanoparticles, all displaying a core-shell morphology. The average diameter of the core-shell nanoparticle is about 10 nm with a shell thickness of 2 nm (Fig 3.C). Additional EELS elemental mapping reveals that elemental composition of the shell includes cobalt, indium and oxygen atoms which agrees with the formation of cobalt-indium oxides.[34] No lattice fringes could be observed in the shell which means that the latter cobalt-indium oxides are also amorphous. On the other hand, the core is clearly polycrystalline as evidenced from the various orientation of lattice fringes

imaged by high-resolution HAADF-STEM (Fig. 4A-C). The high-resolution image of the lattice (Fig. 4C-D) is reproduced by a multi-slice STEM image simulation of a $Co_3InC_{0.75}$ slab viewed along the <110> zone axis (Fig. 4F); the alternance of bright atom columns containing indium and cobalt atoms with fainter atom columns containing only cobalt atoms is especially well reflected.

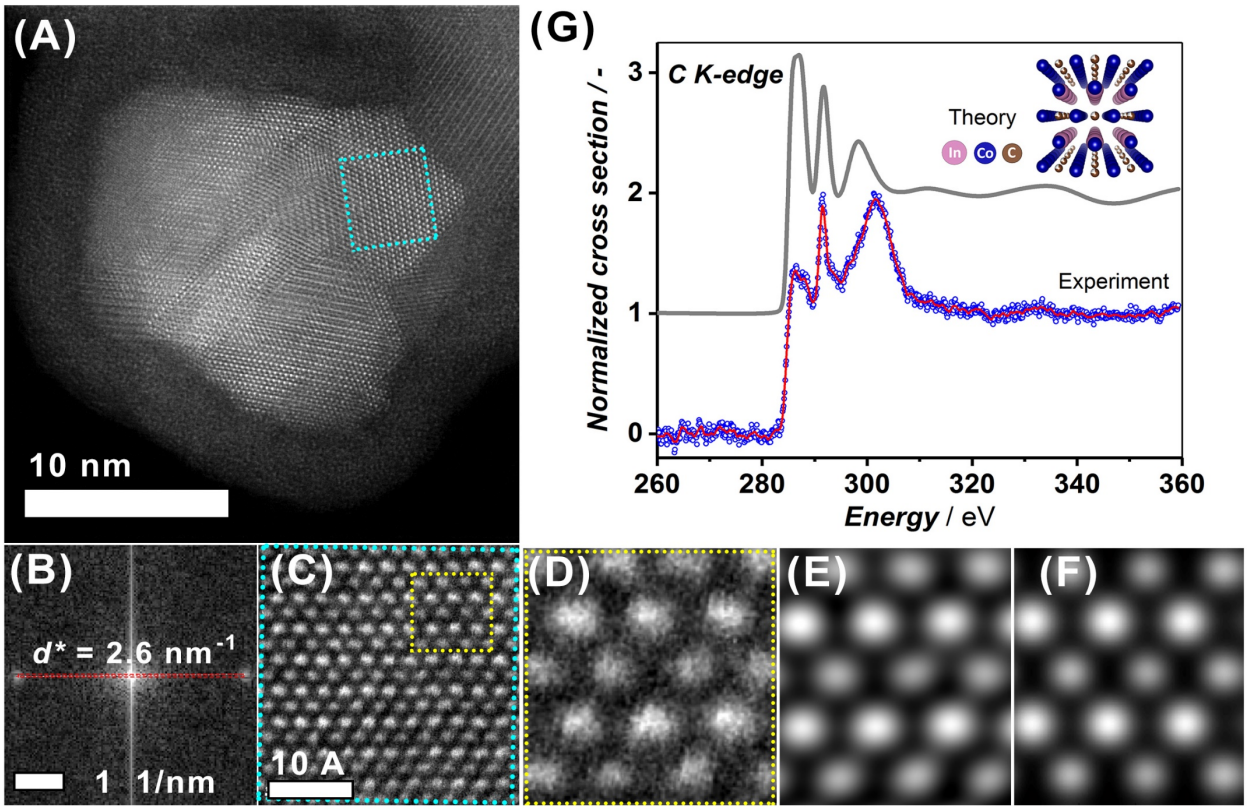

Figure 4. (*double column*). (A) High-resolution HAADF-STEM image of **3**In@**8**Co(300) after reaction. (B) Fourier transform (d^* = 2.6 nm^{-1}, d = 3.83 Å) of (C) zoomed region (blue dots) of interest in (A) representing the atomic arrangement of the $Co_3InC_{0.75}$ phase, viewed along <110> zone axis. (D) Zoomed region in (C, yellow dots) processed with a Wiener and Gaussian band-pass filters (E), and (F) corresponding multi-slice STEM image simulation of a $Co_3InC_{0.75}$ slab. (G) Comparison of experiment and theory (FDMNES calculations) for the carbon K-edge spectrum of $Co_3InC_{0.75}$ recorded by EELS spectroscopy.

With high-angle annular dark field (HAADF) detection, electrons arising from Rutherford scattering are collected, meanwhile electrons deviated by coherent elastic scattering are mostly excluded (removing the phase contrast). The intensity I in the resulting images is then, in a first approximation, given by $I \alpha t \cdot Z^{\alpha}$ ($\alpha = 1.5 - 2$) with a thickness t and an average atomic number Z.[62] As a direct consequence, the difference between indium and cobalt atoms is indeed observable but the carbon atoms located in-between the columns of cobalt atoms are not visualized easily. To definitely support the formation of a mixed carbide phase in the particle core, the carbon K-edge was recorded by EELS spectroscopy (Fig. 4G). The C K-edge originates principally from dipolar transitions from the 1s state to the unoccupied 2*p* state. Unlike X-ray Raman scattering spectroscopy, EELS spectroscopy is highly forward scattered: with a microscope tension of 300 kV, 90% of the intensity is collected within ≈ 2.6 mrad scattering angle corresponding to a small momentum transfer q equal to 0.9 $Å^{-1}$.[63] With those experimental conditions, the monopole transitions ($s \rightarrow s$) are thus neglected.[64] Self-consistent field simulations for $Co_3InC_{0.75}$ clusters with radii of up to 10 Å were performed to ensure the convergence of the calculation. Using the full-potential FDM approach, the three main dipolar transitions observed in the experimental spectra are relatively well reproduced. The agreement is not perfect, especially for the energy position of the third transition, but nevertheless the main features are there.

To summarize, the phase composition of the spent catalyst is dependent of several processes taking place during CO_2 hydrogenation: *i*) the principal process is the formation of $Co_3InC_{0.75}$ constituting the core of catalytically active nanoparticles surrounded by a Co-In oxides shell, *ii*) crystallization of In_2O_3 from amorphous phase as separated nanoparticles, *iii*) reduction of Co_3O_4 to metallic Co.

In order to address the question concerning the relevance of two-step thermal treatment, *i.e.* sequential pyrolysis-calcination process, the catalytic behavior of **3**In@**8**Co(300)-*dc* sample prepared through direct calcination of In-impregnated ZIF-67(Co)-300 at 400 °C without the intermediate pyrolytic step has been evaluated. Kinetic profile of **3**In@**8**Co(300)-*dc* performance in CO_2 hydrogenation towards methanol (Fig. 3A) reveals considerably slower induction period that takes *approx*. 55 h to reach a plateau of 0.28 $g_{MeOH}{\cdot}g_{cat}^{-1}{\cdot}h^{-1}$ STY for the methanol product. Additionally, the catalyst prepared by direct calcination route concedes **3**In@**8**Co(300) material in methanol productivity (0.28 $g_{MeOH}{\cdot}g_{cat}^{-1}{\cdot}h^{-1}$ *vs* 0.52 $g_{MeOH}{\cdot}g_{cat}^{-1}{\cdot}h^{-1}$) albeit with similar S_{MeOH} and higher S_{CO} (Fig. 3A-B). Given the poorer catalytic performance of **3**In@**8**Co(300)-*dc*, one may assume the significance of intermediate pyrolysis step for stabilization of indium and cobalt domains in close vicinity to each other, evidently in form of cobalt indium carbide phase, $Co_3InC_{0.75}$. We presume that such mixed metal carbide redounds the homogeneity of In@Co system after calcination rendering more effective distribution of Co_3O_4 and In_2O_3 oxides within the composite catalyst which, consequently, diminishes the induction period for hydrogenation process.

Taking into account the above-mentioned findings and considering the higher performance of catalyst derived from ZIF-67(Co) sacrificial support with 20 nm crystal size, a set of experiments was carried out in order to study the effect of indium loading. Thereby, ZIF-67(Co)-20 nm has been impregnated with different amounts of $In(NO_3)_3$ in accordance with Table S1 following the same IWI procedure as before and for simplicity denoted as **x**In@**y**Co(20) representing the nominal In:Co molar ratios (x:y) in each sample. As it can be observed from nitrogen absorption measurements (Fig. S22), the shape of isotherms of In@ZIF-67(Co)-20 nm materials changes from type IV- to II- and show the total (BET) surface area descending as the indium content increases

(Table S2, S4). Although indium concentrations were increased gradually, the micropore area deviates from a linear trend; this indicates that the indium species settle not only on external surfaces of ZIF-67(Co) but also occupy the micropore area of the framework.

Afterwards, In@ZIF-67(Co)-20 nm materials with different amounts of loaded indium underwent the sequential pyrolysis-calcination treatment in order to render In@Co composite catalysts. The resulting oxide-containing materials exhibit total surface area ranging from 119 to 87 $m^2 \cdot g^{-1}$ (Table S4) and show II-type adsorption isotherms typical for macroporous adsorbents (Fig. S23). Notably, the total surface area decreases as the indium content increases; that successfully agrees with the findings, above discussed, concerning the embedment of Co_3O_4 nanoparticles possessing the large interparticle surface which is occupied by amorphous In_2O_3 phase. The content of loaded indium in MOF-derived catalysts was confirmed by XRF measurements and calculated from TG curves considering the temperature region of 870-930 °C, in which $Co_3O_4 \rightarrow CoO$ transition is taking place (Figs. S24, S25), in order to compare to the nominal In:Co molar ratios (Table S4). The results summarized in Table S4 show a fair agreement with the expected In:Co ratios aimed to be attained in the **x**In@**y**Co(20) catalysts.

A series of MOF-derived catalysts ***a***In@***b***Co(20) with variable In:Co molar ratios was tested in direct CO_2 hydrogenation to methanol under standard conditions (80%H_2-20%CO_2 feed; P = 50 bar and GHSV = 15600 h^{-1}, Fig. S30). Figure 5A shows kinetic profiles of STY evolution for MeOH product on the catalysts with variable In:Co molar ratios. As can be observed, the ***a***In@***b***Co(20) catalysts with lower In content, *i.e.* **1**In@**23**Co(20) and **1**In@**12**Co(20), exhibit the largest induction periods of 40 and 90 h and a low MeOH productivity of 0.01 and 0.04 $g_{MeOH} \cdot g_{cat}^{-1} \cdot h^{-1}$, respectively. Further increase of indium content up to **1**In:**6**Co value reduces the induction

period down to 30 h yet reaching maximum STY_{MeOH} of 0.21 $g_{MeOH}{\cdot}g_{cat}^{-1}{\cdot}h^{-1}$ over a short period of time (5 h) after which the catalyst slowly deactivates.

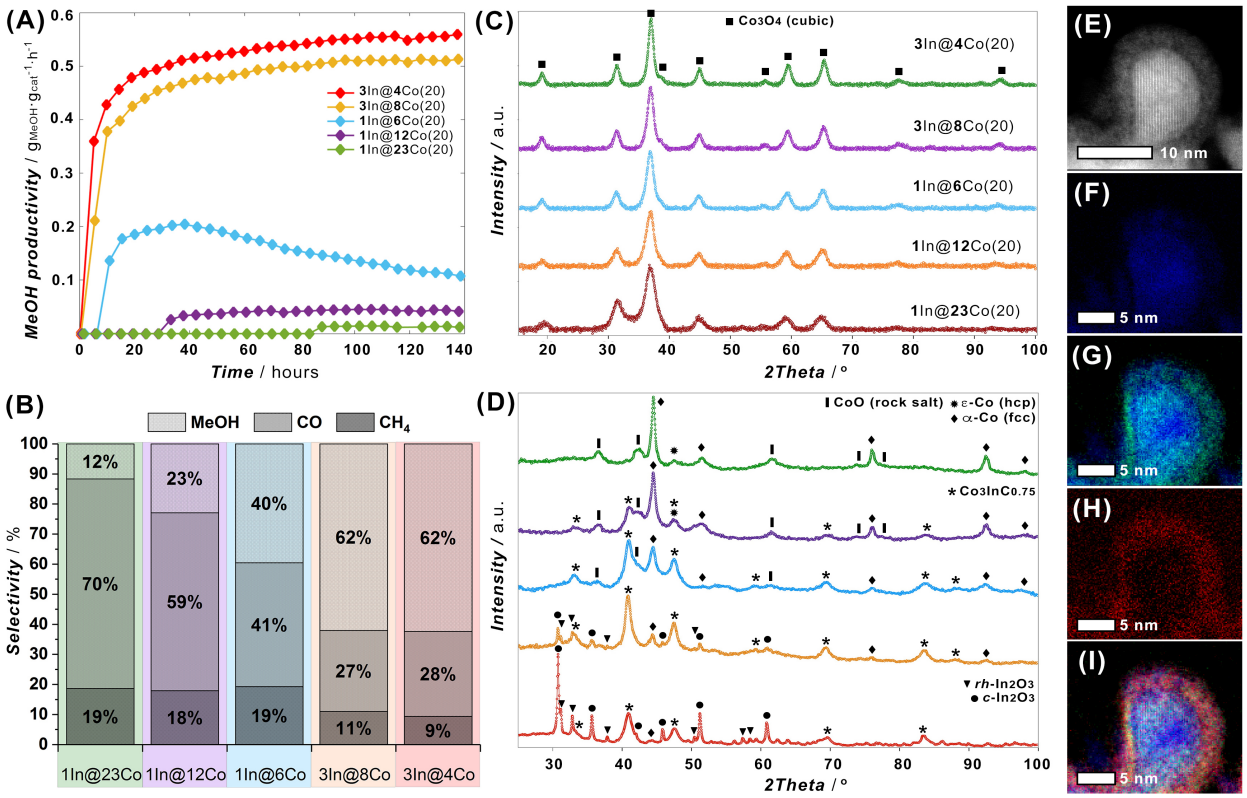

Figure 5. (*double column*). (A) Kinetic profile of evolution MeOH space time yield vs time and (B) selectivities to MeOH product, CO and CH_4 by-products at time-on-stream (*TOS*) of 100 h over catalysts with different In loadings: **3**In@**4**Co(20) (X_{CO2} = 20.5%, red), **3**In@**8**Co(20) (X_{CO2} = 19.2%, orange), **1**In@**6**Co(20) (X_{CO2} = 13.9%, blue), **1**In@**12**Co(20) (X_{CO2} = 11.1%, purple) and **1**In@**23**Co(20) (X_{CO2} = 10.1%, green). Reaction conditions: 80%H_2-20%CO_2 feed; T = 300 °C, P = 50 bar, m_{cat} = 50 mg, GHSV = 15600 h^{-1}. XRD patterns for (C) fresh and (D) spent catalysts and comparison with the identified phases: Co_3O_4 (■), CoO (|), *ε*-Co (hcp,★), $Co_3InC_{0.75}$ (*), *α*-Co (*fcc*,◆), *c*-In_2O_3 (cubic,●) and *rh*-In_2O_3 (rhombohedral,▼). ADF-STEM imaging (E) and

elemental mappings for **3**In@**4**Co(20) after reaction: Co map (F) and O map (H); superimposed Co/In maps (G) and Co/In/O maps (I).

In a contrast, **3**In@**8**Co(20) and **3**In@**4**Co(20) catalysts with higher In_2O_3 loading show considerably reduced induction time (19 h and 7 h *vs* 30 h) and outstanding stable performance over 100 h of reaction with methanol productivity of *ca*. 0.5 and 0.65 $g_{MeOH}{\cdot}g_{cat}^{-1}{\cdot}h^{-1}$, respectively. Therefore, the activity towards methanol product on MOF-derived mixed oxide catalysts is enhancing in order **3**In@**4**Co > **3**In@**8**Co > **1**In@**6**Co > **1**In@**12**Co > **1**In@**23**Co. Regarding the MeOH selectivity data compared at 100 h of time-on-stream (*TOS*) shown on Figure 5B, the methanol selectivity develops following the same trend as STY_{MeOH} whereas the selectivities toward by-products (CO and CH_4) evolve in opposite manner. However, a higher MeOH selectivity (62%) is reached by **3**In@**8**Co(20) and **3**In@**4**Co(20) materials along with reduced selectivities toward CO (27-28%) and CH_4 (9-11%) by-products. In order to understand the differences in reactivity, structural analysis was carried out on the experimental XRD data for fresh and reacted catalysts with different In loadings (Fig. 5C, D). Although the ***a***In@***b***Co(20) catalysts before reaction showed identical XRD pattern with diffraction lines associated solely to the Co_3O_4 phase (Fig. 5C), the composition of reacted solids enriches by diversity of phases, depending on the indium content (Fig. 5C, Table S5). Consequently, the difference in reactivities of the MOF-derived catalysts also relies on the compositional characteristics of the spent phases manifested during the reaction. As shown in Figure 5D, the spent **1**In@**23**Co(20) catalyst mainly contains *fcc*-Co phase and traces of CoO and could be associated with low MeOH selectivity (12 %) and productivity (0.02 $g_{MeOH}{\cdot}g_{cat}^{-1}{\cdot}h^{-1}$) in contrast to high CO selectivity (70 %). The appearance of $Co_3InC_{0.75}$ phase in mixture with *fcc*-Co in **1**In@**12**Co(20) improves the selectivity towards MeOH twofold (S_{MeOH} = 23%, S_{CO} = 59%, S_{CH4} = 18%), whereas the dominance of the mixed-metal carbide

over α-Co in **1**In@**6**Co(20) leads to maximum S_{MeOH} of 40% (S_{CO} = 41%, S_{CH4} = 19%), after which the activity starts to decline. Finally, the mixture of $Co_3InC_{0.75}$ and In_2O_3 (both *rh*- and *c*-polymorphs) more likely reflects the true composition responsible for selective MeOH synthesis inasmuch as both actively performing **3**In@**4**Co(20) and **3**In@**8**Co(20) catalysts possess similar composition based on these two components (S_{MeOH} = 62 %, S_{CO} = 27-28%, S_{CH4} = 9-11% and STY_{MeOH} = 0.5–0.65 $g_{MeOH}{\cdot}g_{cat}^{-1}{\cdot}h^{-1}$). To visualize relations between the phase contents found by PXRD studies, a correlation matrix has been added (Fig. S31). The correlation coefficients between individual phase contents and selectivities towards the catalytic products were scaled from yellow (strong positive) to navy (strong negative correlation). It demonstrates strong correlation between the carbide and indium oxides content and methanol selectivity whereas cobalt and cobalt oxide presence negatively correlated with it. Although carbide content has the strongest correlation with methanol production, its catalytic activity was excluded by performing an individual catalytic study (Table S7) and appeared to be a side product of catalysts workout and carburization (Figs. S35-S38). To support the above-mentioned results, CHN elemental analyses on the fresh and spent catalysts were carried out and compared in Table S6. As expected, the carbon content in reacted catalysts increases compared to the fresh ones and can be associated with the formation of $Co_3InC_{0.75}$ phase; that agrees well with PXRD quantification data (Table S5). Notably, spent **3**In@**4**Co(20) and **3**In@**8**Co(20) catalysts differ by relative amount of crystalline In_2O_3 and $Co_3InC_{0.75}$ phases (Table S5) that might have influence on the induction period considering previous finding that both components are formed along the sequentially-conjugated process. Similarly to **3**In@**8**Co(300), the spent version of the best performing **3**In@**4**Co(20) catalyst shows also core-shell morphological features as suggested by EELS elemental maps (Figs. 5E-I, Figs. S26-S27). In conclusion to all above mentioned, the optimal catalyst composition is

determined by relative molar ratio of **3**In:**8**Co and **3**In:**4**Co possessing enough indium to be quantitatively converted to $Co_3InC_{0.75}$ phase.

The most active catalysts, **3**In@**4**Co(20) and **3**In@**8**Co(20), were chosen to study the effect of the reaction temperature with the aim of finding optimal conditions for CO_2 to methanol hydrogenation process. The kinetic profiles for MeOH productivity on **3**In@**4**Co(20) and **3**In@**8**Co(20) catalysts at three temperatures – 270 °C, 285 °C and 300 °C, are shown in Figure 6A. As can be observed, the induction period for both catalysts increases from 7-19 h to 60-70 h while the reaction temperature decreases from 300 °C to 270°C. This observation can be rationalized by the fact that both $Co_3InC_{0.75}$ and In_2O_3 phases formed through conjugated red-ox process become kinetically unfavorable at lower temperatures. Despite the discrepancy of initial reaction rates for both catalysts, the MeOH productivity is deviating in a range of 0.5–0.65 $g_{MeOH} \cdot g_{cat}^{-1} \cdot h^{-1}$ regardless the applied temperature. However, the alternate comparison of selectivities for MeOH product and CO/CH_4 by-products in the steady-state region (Fig. 6B, Fig. S32) of the catalytic process shows that lower temperature induces high methanol selectivities (S_{MeOH} ~ 79-80% at 270 °C vs 62 % at 300 °C) yet suppresses side processes (S_{CO} ~ 15 % and S_{CH4} ~ 5 % at 270 °C *vs* S_{CO} ~ 27-28 % and S_{CH4} ~ 9-11 % at 300 °C), *i.e.* methanation and reverse water-gas shift (RWGS) reactions.

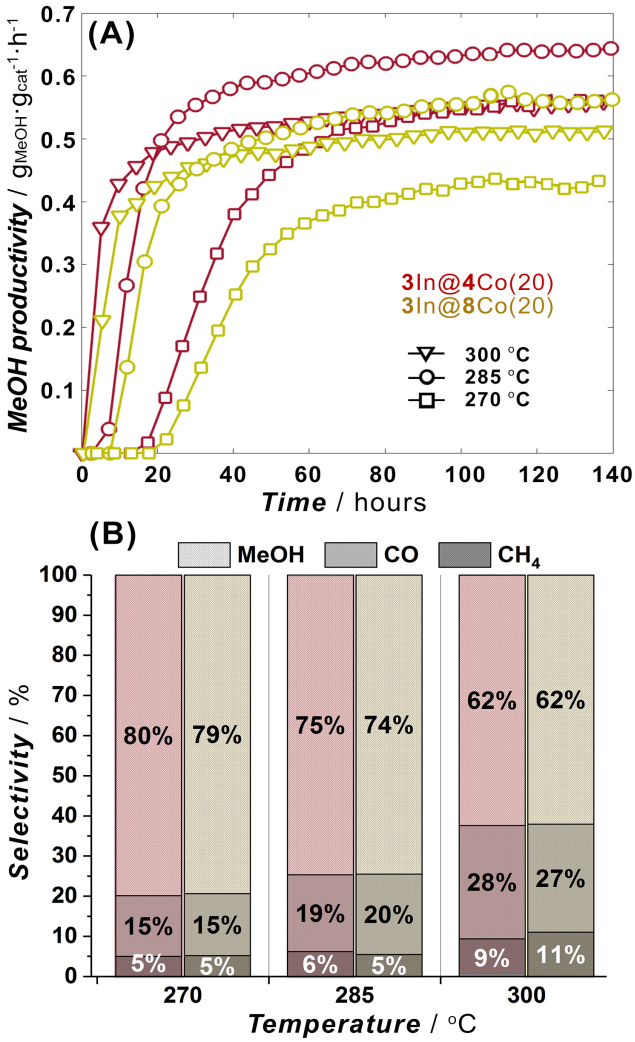

Figure 6. (*single column*). (A) Kinetic profile of evolution MeOH space time yield *vs* time and (B) selectivities to MeOH product, CO and CH_4 by-products at time-on-stream (*TOS*) of 100 h over catalysts **3**In@**4**Co(20) (red) and **3**In@**8**Co(20) (orange) at different temperatures: 270 ºC ((X_{CO2} = 14.2% and 11.6%, □), 285 ºC (X_{CO2} = 17.3% and 15.5%, ○) and 300 ºC (X_{CO2} = 20.5% and 19.2%, ▽). Reaction conditions: 80%H_2-20%CO_2 feed; P = 50 bar, m_{cat} = 50 mg, GHSV = 15600 h^{-1}.

Thus, an optimal temperature needs to be considered in order to inhibit undesired side reactions and favor higher methanol selectivity and productivity yield.

Additionally, in order to tune the reaction performance, we carried out a series of experiments with variable gas flows, given the fact that RWGS and methanation processes may be suppressed to some extent this way. Figure 7A shows the **3**In@**4**Co(20) catalyst performance on stream at 270 °C under different gas flow velocities (GHSV, h^{-1}).

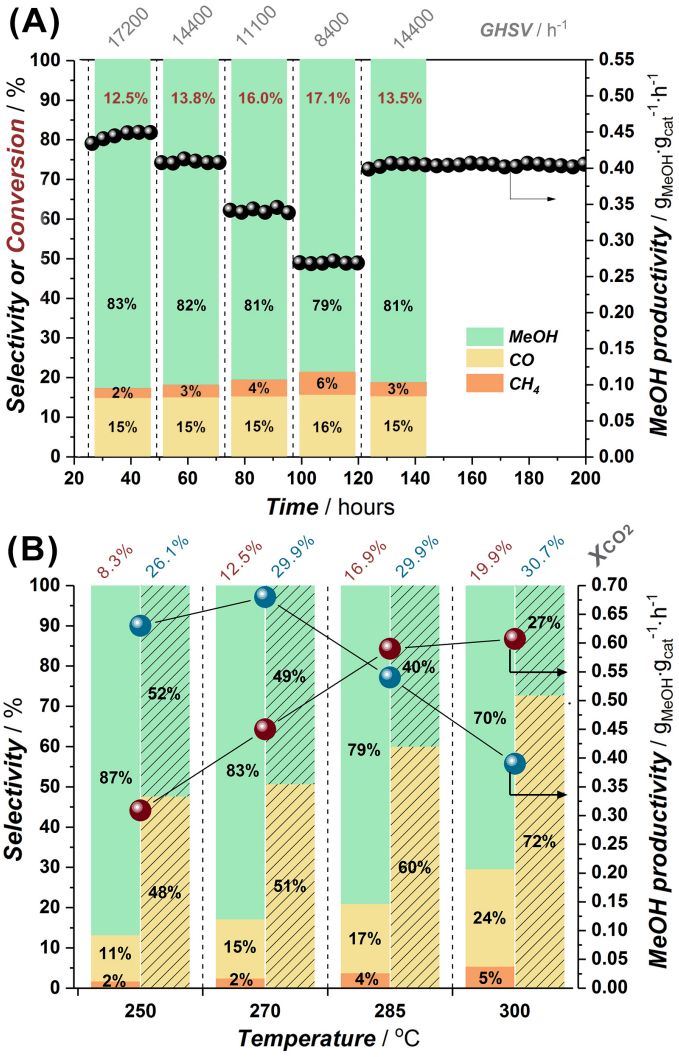

Figure 7. (*single column*). (A) Evolution selectivities for MeOH product (turquoise column), CO (orange) and CH_4 (pumpkin) by-products, CO_2 conversion (wine values) and MeOH space time yield (black spheres) *vs* time on catalyst **3**In@**4**Co(20) at variable GHSV (top, grey values) and 270 °C. Catalyst was previously pretreated at 300 °C and GHSV of 15200 h^{-1} for 20 h in the

reaction mixture. (B) Comparison of methanol productivity (spheres) and MeOH, CO and CH_4 selectivities (columns) for **3**In@**4**Co(20) (red markers and clear columns) and commercial Cu-ZnO-Al_2O_3 catalyst (blue markers and striped columns) at 250 °C, 270 °C, 285 °C, 300 °C and constant GHSV of 17200 h^{-1}, X_{CO2} levels are represented on the line above. Reaction conditions: 80%H_2-20%CO_2 feed; P = 50 bar, m_{cat} = 50 mg.

As can be observed in Figure 7A, after catalyst pretreatment at 300 °C for 20 h, the increase of the contact time leads to growth in the productivity and methanol selectivity reaching of MeOH productivity (0.45 $g_{MeOH}{\cdot}g_{cat}^{-1}{\cdot}h^{-1}$) and selectivity (83%) at 17200 h^{-1}. This behavior is in line with the previously observed for In-based catalyst by Pérez-Ramírez *et. al.*[32] Expectedly, this outcome runs in parallel with inhibition of side reactions showing decrease of CO and CH_4 selectivities down to 2% and 15%, respectively. Although the subsequent stepwise reduction of GHSV from 17200 h^{-1} to 8400 h^{-1} diminishes MeOH productivity drastically (from 0.45 $g_{MeOH}{\cdot}g_{cat}^{-1}{\cdot}h^{-1}$ to 0.27 $g_{MeOH}{\cdot}g_{cat}^{-1}{\cdot}h^{-1}$), the selectivities toward methanol lessen slowly from 83% to 79%. It is worth to note that when GHSV is restored to 14400 h^{-1}, **3**In@**4**Co(20) catalyst could recover its activity reaching the same MeOH productivity (0.40 $g_{MeOH}{\cdot}g_{cat}^{-1}{\cdot}h^{-1}$) and selectivities ($S_{MeOH}$ = 81% *vs* 82%). This observation highlights the stability of MOF-derived In@Co composite catalyst over the course of the reaction and instant response to the changes in the reaction conditions.

To have an accurate comparison of catalytic activity for our MOF-derived composite catalyst, **3**In@**4**Co(20) with the commercial Cu-ZnO-Al_2O_3, we performed an extensive examination of both solids in CO_2 hydrogenation under different reaction conditions (Fig. S33-S34). Since it was determined that the GHSV directly influences the methanol yield and selectivity, further comparison has been done at fixed gas velocity (17 200 h^{-1}) at which both catalysts performed best. Accordingly, the general trends observed in both catalytic systems are summarized in Figure 7B.

The results show two distinct regimes – above and below *ca*. 280 °C. In low temperature regime (< 280 °C), the commercial Cu-ZnO-Al_2O_3 catalyst shows considerably high MeOH yield (0.65-0.67 $g_{MeOH}{\cdot}g_{cat}^{-1}{\cdot}h^{-1}$) with moderate product selectivities (S_{MeOH} = 49-52% and S_{CO} = 48-51%) whereas MOF-derived **3**In@**4**Co(20) composite exhibits lower MeOH productivity (0.32-0.45 $g_{MeOH}{\cdot}g_{cat}^{-1}{\cdot}h^{-1}$) with remarkably higher selectivity (83-87%) towards the desired product. In contrast, the high temperature regime (> 280 °C) turns the overall catalytic performance in opposite direction where **3**In@**4**Co(20) catalyst reaches the maximum of STY_{MeOH} (0.60-0.63 $g_{MeOH}{\cdot}g_{cat}^{-1}{\cdot}h^{-1}$) with slightly lower methanol selectivity (70-79%), yet much higher than that of the Cu-ZnO-Al_2O_3.

4. Conclusions

In this work we have applied the MOF-mediated approach to prepare In_2O_3-Co_3O_4 mixed-oxide catalysts for the effective and selective synthesis of methanol *via* CO_2 hydrogenation. The activity of the resulting In@Co catalysts reaches a maximum MeOH space time yield of 0.65 $g_{MeOH}{\cdot}g_{cat}^{-1}{\cdot}h^{-1}$ with methanol selectivities as high as 87% over 100 h on stream under industrially relevant conditions. Owing to the relatively slow kinetics of active phase formation in co-precipitated In@Co catalytic system previously reported, the induction period for the hydrogenation process on the catalysts prepared by MOF-mediated approach could be tuned by changes of the textural properties of parent sacrificial ZIF-67(Co) support providing better In dopant distribution all over the metal-organic matrix involving both micropore and interparticle surface areas, improving in this way In utilization. Additionally, we found the relevance of the sequential pyrolysis-calcination steps in the catalysts' preparation procedure to be determinant for faster induction period due to appearance of mixed-metal carbide, $Co_3InC_{0.75}$, which stabilizes high dopant distribution and prevents formation of large individual oxide domains in the final mixed oxide composite. As

expected, the indium loading implies the quantitative limitation on formation of the active phase, which presumably consists of nanoparticles featuring core-shell morphologies (Co-In oxides shell over $Co_3InC_{0.75}$ core) hereby establishing optimal composition of **3**In:**8**Co or **3**In:**4**Co molar ratios for more effective catalyst performance.

The screening for the optimal operational conditions shows that lower reaction temperature assists to suppress side reactions (methanation and RWGS) and improve MeOH selectivity (S_{MeOH} ~ 79-80% at 270 °C *vs* 62 % at 300 °C) while slightly lowering the productivity (0.55 $g_{MeOH}{\cdot}g_{cat}^{-1}{\cdot}h^{-1}$ at 270 °C *vs* 0.65 $g_{MeOH}{\cdot}g_{cat}^{-1}{\cdot}h^{-1}$ at 300 °C). Additionally, further annihilation of undesired side processes (methanation and RWGS) could be reached by adjusting the reaction conditions, *i.e.* reactant gas flow, lowering S_{CO} and S_{CH4} down to 11 and 2%, respectively.

The present study demonstrates the tunability of MOF-mediated approach of preparation of In_2O_3-Co_3O_4 catalytic system which is able to drive effectively direct CO_2 hydrogenation to methanol. Our results suggest that In@Co binary oxide system is able to reach superior performance compared to commercial Cu-ZnO-Al_2O_3 catalyst for this reaction.

AUTHOR INFORMATION

Corresponding Author

* jorge.gascon@kaust.edu.sa

Present Addresses

† King Abdullah University of Science and Technology, KAUST Catalysis Center (KCC), Advanced Catalytic Materials, Thuwal 23955, Saudi Arabia

§ Néel, UPR2940 CNRS, University of Grenoble Alpes, F-38000 Grenoble, France

Author Contributions

The manuscript was written through contributions of all authors. All authors have given approval to the final version of the manuscript.

Funding Sources

Funding for this work was provided by King Abdullah University of Science and Technology (KAUST).

ASSOCIATED CONTENT

Supporting Information.

The following file are available free of charge.

Transmission electron microscopy images, EELS elemental mappings, thermogravimetric analyses, BET results, catalytic data, catalyst characterization by the means of XRD, CHN, XRF, XAS techniques (PDF).

ACKNOWLEDGMENT

The authors gratefully acknowledge the European Synchrotron Radiation Facility (Grenoble, France) for provision of beamtime (CH-5572) for XAS experiments carried out on the FAME beamline (BM30B) and support of their staff.

REFERENCES

(1) Fankhauser, S.; Jotzo, F., Economic Growth and Development with Low-Carbon Energy, *Wiley Interdiscip. Rev. Clim. Change* **2018,** 9, e495.
(2) Olah, G. A.; Goeppert, A.; Prakash, G. K. S., Chemical Recycling of Carbon Dioxide to Methanol and Dimethyl Ether: From Greenhouse Gas to Renewable, Environmentally Carbon Neutral Fuels and Synthetic Hydrocarbons, *J. Org. Chem.* **2009,** 74, 487-498.

(3) Rafiee, A.; Rajab Khalilpour, K.; Milani, D.; Panahi, M., Trends in CO_2 Conversion and Utilization: A Review from Process Systems Perspective, *J. Environ. Chem. Eng.* **2018,** 6, 5771-5794.
(4) Dokania, A.; Ramirez, A.; Bavykina, A.; Gascon, J., Heterogeneous Catalysis for the Valorization of CO_2: Role of Bifunctional Processes in the Production of Chemicals, *ACS Energy Lett.* **2019,** 4, 167-176.
(5) Olah, G. A., Beyond Oil and Gas: The Methanol Economy, *Angew. Chem., Int. Ed.* **2005,** 44, 2636-2639.
(6) Zhen, X. In *Methanol*, Basile, A., Dalena, F., Eds. Elsevier: 2018; pp 313-337.
(7) Tian, P.; Wei, Y.; Ye, M.; Liu, Z., Methanol to Olefins (MTO): From Fundamentals to Commercialization, *ACS Catal.* **2015,** 5, 1922-1938.
(8) Yarulina, I.; De Wispelaere, K.; Bailleul, S.; Goetze, J.; Radersma, M.; Abou-Hamad, E.; Vollmer, I.; Goesten, M.; Mezari, B.; Hensen, E. J. M.; Martínez-Espín, J. S.; Morten, M.; Mitchell, S.; Perez-Ramirez, J.; Olsbye, U.; Weckhuysen, B. M.; Van Speybroeck, V.; Kapteijn, F.; Gascon, J., Structure–Performance Descriptors and the Role of Lewis Acidity in the Methanol-to-Propylene Process, *Nat. Chem.* **2018,** 10, 804-812.
(9) Dutta, A.; Karimi, I. A.; Farooq, S., Technoeconomic Perspective on Natural Gas Liquids and Methanol as Potential Feedstocks for Producing Olefins, *Ind. Eng. Chem. Res.* **2019,** 58, 963-972.
(10) Yarulina, I.; Chowdhury, A. D.; Meirer, F.; Weckhuysen, B. M.; Gascon, J., Recent Trends and Fundamental Insights in the Methanol-to-Hydrocarbons Process, *Nat. Catal.* **2018,** 1, 398-411.
(11) Álvarez, A.; Bansode, A.; Urakawa, A.; Bavykina, A. V.; Wezendonk, T. A.; Makkee, M.; Gascon, J.; Kapteijn, F., Challenges in the Greener Production of Formates/Formic Acid, Methanol, and DME by Heterogeneously Catalyzed CO_2 Hydrogenation Processes, *Chem. Rev.* **2017,** 117, 9804-9838.
(12) Kiss, A. A.; Pragt, J. J.; Vos, H. J.; Bargeman, G.; de Groot, M. T., Novel Efficient Process for Methanol Synthesis by CO_2 Hydrogenation, *Chem. Eng. J.* **2016,** 284, 260-269.
(13) González-Garay, A.; Frei, M. S.; Al-Qahtani, A.; Mondelli, C.; Guillén-Gosálbez, G.; Pérez-Ramírez, J., Plant-to-Planet Analysis of CO_2-Based Methanol Processes, *Energy Environ. Sci.* **2019**, 12, 3425-3436.
(14) Ali, K. A.; Abdullah, A. Z.; Mohamed, A. R., Recent Development in Catalytic Technologies for Methanol Synthesis from Renewable Sources: A Critical Review, *Renewable Sustainable Energy Rev.* **2015,** 44, 508-518.
(15) Martin, O.; Pérez-Ramírez, J., New and Revisited Insights into the Promotion of Methanol Synthesis Catalysts by CO_2, *Catal. Sci. Technol.* **2013,** 3, 3343-3352.
(16) Wu, J.; Saito, M.; Takeuchi, M.; Watanabe, T., The Stability of Cu/ZnO-Based Catalysts in Methanol Synthesis from a CO_2-Rich Feed and from a CO-Rich Feed, *Appl. Catal., A* **2001,** 218, 235-240.
(17) Ash-Kurlander, U.; Martin, O.; Fontana, L. D.; Patil, V. R.; Bernegger, M.; Mondelli, C.; Pérez-Ramírez, J.; Steinfeld, A., Impact of Daily Startup–Shutdown Conditions on the Production of Solar Methanol over a Commercial Cu–ZnO–Al_2O_3 Catalyst, *Energy Technol.* **2016,** 4, 565-572.
(18) Arena, F.; Barbera, K.; Italiano, G.; Bonura, G.; Spadaro, L.; Frusteri, F., Synthesis, Characterization and Activity Pattern of Cu–ZnO/ZrO_2 Catalysts in the Hydrogenation of Carbon Dioxide to Methanol, *J. Catal.* **2007,** 249, 185-194.

(19) Porosoff, M. D.; Yan, B.; Chen, J. G., Catalytic Reduction of CO_2 by H_2 for Synthesis of CO, Methanol and Hydrocarbons: Challenges and Opportunities, *Energy Environ. Sci.* **2016,** 9, 62-73.
(20) Bansode, A.; Urakawa, A., Towards Full One-Pass Conversion of Carbon Dioxide to Methanol and Methanol-Derived Products, *J. Catal.* **2014,** 309, 66-70.
(21) Le Valant, A.; Comminges, C.; Tisseraud, C.; Canaff, C.; Pinard, L.; Pouilloux, Y., The Cu–ZnO Synergy in Methanol Synthesis from CO_2, Part 1: Origin of Active Site Explained by Experimental Studies and a Sphere Contact Quantification Model on Cu+ZnO Mechanical Mixtures, *J. Catal.* **2015,** 324, 41-49.
(22) Tada, S.; Watanabe, F.; Kiyota, K.; Shimoda, N.; Hayashi, R.; Takahashi, M.; Nariyuki, A.; Igarashi, A.; Satokawa, S., Ag Addition to CuO-ZrO_2 Catalysts Promotes Methanol Synthesis via CO_2 Hydrogenation, *J. Catal.* **2017,** 351, 107-118.
(23) Köck, E.-M.; Kogler, M.; Grünbacher, M.; Zhuo, C.; Thalinger, R.; Schmidmair, D.; Schlicker, L.; Gurlo, A.; Penner, S., Metastable Corundum-Type In_2O_3: Phase Stability, Reduction Properties, and Catalytic Characterization, *J. Phys. Chem. C* **2016,** 120, 15272-15281.
(24) Hu, B.; Yin, Y.; Liu, G.; Chen, S.; Hong, X.; Tsang, S. C. E., Hydrogen Spillover Enabled Active Cu Sites for Methanol Synthesis from CO_2 Hydrogenation over Pd Doped CuZn Catalysts, *J. Catal.* **2018,** 359, 17-26.
(25) Dang, S.; Yang, H.; Gao, P.; Wang, H.; Li, X.; Wei, W.; Sun, Y., A Review of Research Progress on Heterogeneous Catalysts for Methanol Synthesis from Carbon Dioxide Hydrogenation, *Catal. Today* **2019,** 330, 61-75.
(26) Jadhav, S. G.; Vaidya, P. D.; Bhanage, B. M.; Joshi, J. B., Catalytic Carbon Dioxide Hydrogenation to Methanol: A Review of Recent Studies, *Chem. Eng. Res. Des.* **2014,** 92, 2557-2567.
(27) Słoczyński, J.; Grabowski, R.; Kozłowska, A.; Olszewski, P.; Stoch, J.; Skrzypek, J.; Lachowska, M., Catalytic Activity of the M/(3ZnO·ZrO_2) System (M=Cu, Ag, Au) in the Hydrogenation of CO_2 to Methanol, *Appl. Catal. A* **2004,** 278, 11-23.
(28) Bansode, A.; Tidona, B.; von Rohr, P. R.; Urakawa, A., Impact of K and Ba Promoters on CO_2 Hydrogenation over Cu/Al_2O_3 Catalysts at High Pressure, *Catal. Sci. Technol.* **2013,** 3, 767-778.
(29) Gao, P.; Li, F.; Zhao, N.; Xiao, F.; Wei, W.; Zhong, L.; Sun, Y., Influence of Modifier (Mn, La, Ce, Zr and Y) on the Performance of Cu/Zn/Al Catalysts via Hydrotalcite-Like Precursors for CO_2 Hydrogenation to Methanol, *Appl. Catal. A* **2013,** 468, 442-452.
(30) Ye, J.; Liu, C.; Mei, D.; Ge, Q., Active Oxygen Vacancy Site for Methanol Synthesis from CO_2 Hydrogenation on In_2O_3(110): a DFT Study, *ACS Catal.* **2013,** 3, 1296-1306.
(31) Sun, K.; Fan, Z.; Ye, J.; Yan, J.; Ge, Q.; Li, Y.; He, W.; Yang, W.; Liu, C.-J., Hydrogenation of CO_2 to Methanol over In_2O_3 Catalyst, *J. CO_2 Util.* **2015,** 12, 1-6.
(32) Martin, O.; Martín, A. J.; Mondelli, C.; Mitchell, S.; Segawa, T. F.; Hauert, R.; Drouilly, C.; Curulla-Ferré, D.; Pérez-Ramírez, J., Indium Oxide as a Superior Catalyst for Methanol Synthesis by CO_2 Hydrogenation, *Angew. Chem., Int. Ed.* **2016,** 55, 6261-6265.
(33) Frei, M. S.; Mondelli, C.; García-Muelas, R.; Kley, K. S.; Puértolas, B.; López, N.; Safonova, O. V.; Stewart, J. A.; Curulla Ferré, D.; Pérez-Ramírez, J., Atomic-Scale Engineering of Indium Oxide Promotion by Palladium for Methanol Production via CO_2 Hydrogenation, *Nat. Commun.* **2019**, 10, 3377.
(34) Bavykina, A.; Yarulina, I.; Al Abdulghani, A. J.; Gevers, L.; Hedhili, M. N.; Miao, X. H.; Galilea, A. R.; Pustovarenko, A.; Dikhtiarenko, A.; Cadiau, A.; Aguilar-Tapia, A.; Hazemann, J.

L.; Kozlov, S. M.; Oud-Chikh, S.; Cavallo, L.; Gascon, J., Turning a Methanation Co Catalyst into an In-Co Methanol Producer, *ACS Catal*. **2019,** 9, 6910-6918.
(35) Li, G.; Zhao, S.; Zhang, Y.; Tang, Z., Metal–Organic Frameworks Encapsulating Active Nanoparticles as Emerging Composites for Catalysis: Recent Progress and Perspectives, *Adv. Mater*. **2018,** 30, 1800702.
(36) Drake, T.; Ji, P.; Lin, W., Site Isolation in Metal–Organic Frameworks Enables Novel Transition Metal Catalysis, *Acc. Chem. Res*. **2018,** 51, 2129-2138.
(37) Zhao, S.-N.; Song, X.-Z.; Song, S.-Y.; Zhang, H.-j., Highly Efficient Heterogeneous Catalytic Materials Derived from Metal-Organic Framework Supports/Precursors, *Coord. Chem. Rev*. **2017,** 337, 80-96.
(38) Furukawa, H.; Cordova, K. E.; O'Keeffe, M.; Yaghi, O. M., The Chemistry and Applications of Metal-Organic Frameworks, *Science* **2013,** 341, 1230444.
(39) An, B.; Zhang, J.; Cheng, K.; Ji, P.; Wang, C.; Lin, W., Confinement of Ultrasmall Cu/ZnO_x Nanoparticles in Metal–Organic Frameworks for Selective Methanol Synthesis from Catalytic Hydrogenation of CO_2, *J. Am. Chem. Soc*. **2017,** 139, 3834-3840.
(40) Rungtaweevoranit, B.; Baek, J.; Araujo, J. R.; Archanjo, B. S.; Choi, K. M.; Yaghi, O. M.; Somorjai, G. A., Copper Nanocrystals Encapsulated in Zr-Based Metal–Organic Frameworks for Highly Selective CO_2 Hydrogenation to Methanol, *Nano Lett*. **2016,** 16, 7645-7649.
(41) Oar-Arteta, L.; Wezendonk, T.; Sun, X.; Kapteijn, F.; Gascon, J. In *Nanotechnology in Catalysis*, John Wiley & Sons, Ltd: 2017; pp 225-250.
(42) Oar-Arteta, L.; Wezendonk, T.; Sun, X.; Kapteijn, F.; Gascon, J., Metal Organic Frameworks as Precursors for the Manufacture of Advanced Catalytic Materials, *Mater. Chem. Front*. **2017,** 1, 1709-1745.
(43) Xia, W.; Zhu, J.; Guo, W.; An, L.; Xia, D.; Zou, R., Well-Defined Carbon Polyhedrons Prepared from Nano Metal-Organic Frameworks for Oxygen Reduction, *J. Mater. Chem. A* **2014,** 2, 11606-11613.
(44) Sun, X.; Suarez, A. I. O.; Meijerink, M.; van Deelen, T.; Ould-Chikh, S.; Zečević, J.; de Jong, K. P.; Kapteijn, F.; Gascon, J., Manufacture of Highly Loaded Silica-Supported Cobalt Fischer–Tropsch Catalysts from a Metal Organic Framework, *Nat. Commun*. **2017,** 8, 1680.
(45) Pawley, G., Unit-Cell Refinement from Powder Diffraction Scans, *J. Appl. Crystallogr*. **1981,** 14, 357-361.
(46) Coelho, A., TOPAS and TOPAS-Academic: An Optimization Program Integrating Computer Algebra and Crystallographic Objects Written in C^{++}, *J. Appl. Crystallogr*. **2018,** 51, 210-218.
(47) Schindelin, J.; Arganda-Carreras, I.; Frise, E.; Kaynig, V.; Longair, M.; Pietzsch, T.; Preibisch, S.; Rueden, C.; Saalfeld, S.; Schmid, B.; Tinevez, J.-Y.; White, D. J.; Hartenstein, V.; Eliceiri, K.; Tomancak, P.; Cardona, A., Fiji: An Open-Source Platform for Biological-Image Analysis, *Nat. Methods* **2012,** 9, 676.
(48) Ravel, B.; Newville, M., Athena, Artemis, Hephaestus: Data Analysis for X-Ray Absorption Spectroscopy Using IFEFFIT, *J. Synchrotron Radiat*. **2005,** 12, 537-541.
(49) Koch, C. T., in *Determination of Core Structure Periodicity and Point Defect Density Along Dislocations*. 2002.
(50) Bunău, O.; Joly, Y., Self-Consistent Aspects of X-Ray Absorption Calculations, *J. Phys. Condens. Matter* **2009,** 21, 345501.
(51) Guda, S. A.; Guda, A. A.; Soldatov, M. A.; Lomachenko, K. A.; Bugaev, A. L.; Lamberti, C.; Gawelda, W.; Bressler, C.; Smolentsev, G.; Soldatov, A. V.; Joly, Y., Optimized Finite

Difference Method for the Full-Potential XANES Simulations: Application to Molecular Adsorption Geometries in MOFs and Metal–Ligand Intersystem Crossing Transients, *J. Chem. Theory Comput.* **2015,** 11, 4512-4521.
(52) Banerjee, R.; Phan, A.; Wang, B.; Knobler, C.; Furukawa, H.; O'Keeffe, M.; Yaghi, O. M., High-Throughput Synthesis of Zeolitic Imidazolate Frameworks and Application to CO_2 Capture, *Science* **2008,** 319, 939-943.
(53) Kwon, H. T.; Jeong, H.-K.; Lee, A. S.; An, H. S.; Lee, J. S., Heteroepitaxially Grown Zeolitic Imidazolate Framework Membranes with Unprecedented Propylene/Propane Separation Performances, *J. Am. Chem. Soc.* **2015,** 137, 12304-12311.
(54) Thommes, M., Physical Adsorption Characterization of Nanoporous Materials, *Chem. Ing. Tech.* **2010,** 82, 1059-1073.
(55) Sing, K. S. W., Reporting Physisorption Data for Gas/Solid Systems with Special Reference to the Determination of Surface Area and Porosity (Recommendations 1984), *Pure Appl. Chem.* **1985,** 57, 603-619.
(56) In *Thermodynamic Properties of Elements, Ca to Ge2: Datasheet from Landolt-Börnstein - Group Iv Physical Chemistry*, Hurtado, I., Neuschütz, D., Eds. Springer-Verlag Berlin Heidelberg: 1999; Vol. 19A1.
(57) P. Xu, Z.; C. Zeng, H., Thermal Evolution of Cobalt Hydroxides: A Comparative Study of Their Various Structural Phases, *J. Mater. Chem.* **1998,** 8, 2499-2506.
(58) Marezio, M., Refinement of the Crystal Structure of In_2O_3 at Two Wavelengths, *Acta Crystallogr.* **1966,** 20, 723-728.
(59) Gurlo, A.; Kroll, P.; Riedel, R., Metastability of Corundum-Type In_2O_3, *Chem. – Eur. J.* **2008,** 14, 3306-3310.
(60) Bekheet, M. F.; Schwarz, M. R.; Kroll, P.; Gurlo, A., Kinetic Control in the Synthesis of Metastable Polymorphs: Bixbyite-to-Rh_2O_3(II)-to-Corundum Transition in In_2O_3, *J. Solid State Chem.* **2015,** 229, 278-286.
(61) Köck, E.-M.; Kogler, M.; Zhuo, C.; Schlicker, L.; Bekheet, M. F.; Doran, A.; Gurlo, A.; Penner, S., Surface Chemistry and Stability of Metastable Corundum-Type In_2O_3, *Phys. Chem. Chem. Phys.* **2017,** 19, 19407-19419.
(62) Crewe, A. V.; Wall, J.; Langmore, J., Visibility of Single Atoms, *Science* **1970,** 168, 1338-1340.
(63) Egerton, R. F., *Electron Energy-Loss Spectroscopy in the Electron Microscope*. 2nd ed.; Plenum Press: 1996.
(64) Joly, Y.; Cavallari, C.; Guda, S. A.; Sahle, C. J., Full-Potential Simulation of X-Ray Raman Scattering Spectroscopy, *J. Chem. Theory Comput.* **2017,** 13, 2172-2177.

TABLE OF CONTENT (TOC)